ELSEVIER

Journal of Neuroscience Methods 154 (2006) 161–174

JOURNAL OF NEUROSCIENCE METHODS

www.elsevier.com/locate/jneumeth

Ultrafast random-access scanning in two-photon microscopy using acousto-optic deflectors

R. Salomé [a,1], Y. Kremer [a,1], S. Dieudonné [a], J.-F. Léger [a], O. Krichevsky [c], C. Wyart [a], D. Chatenay [b], L. Bourdieu [a,*]

[a] *Laboratoire de Neurobiologie Moléculaire et Cellulaire, UMR CNRS 8544, Ecole Normale Supérieure, Département de Biologie, 46 rue d'Ulm, 75005 Paris, France*

[b] *Laboratoire de Physique Statistique, UMR CNRS 8550, Ecole Normale Supérieure, Département de Physique, 24 rue Lhomond, 75005 Paris, France*

[c] *Physics Department, Ben-Gurion University, P.O.B. 653, Beer-Sheva 84105, Israel*

Received 26 August 2005; received in revised form 10 December 2005; accepted 10 December 2005

Abstract

Two-photon scanning microscopy (TPSM) is a powerful tool for imaging deep inside living tissues with sub-cellular resolution. The temporal resolution of TPSM is however strongly limited by the galvanometric mirrors used to steer the laser beam. Fast physiological events can therefore only be followed by scanning repeatedly a single line within the field of view. Because acousto-optic deflectors (AODs) are non-mechanical devices, they allow access at any point within the field of view on a microsecond time scale and are therefore excellent candidates to improve the temporal resolution of TPSM. However, the use of AOD-based scanners with femtosecond pulses raises several technical difficulties. In this paper, we describe an all-digital TPSM setup based on two crossed AODs. It includes in particular an acousto-optic modulator (AOM) placed at 45° with respect to the AODs to pre-compensate for the large spatial distortions of femtosecond pulses occurring in the AODs, in order to optimize the spatial resolution and the fluorescence excitation. Our setup allows recording from freely selectable point-of-interest at high speed (1 kHz). By maximizing the time spent on points of interest, random-access TPSM (RA-TPSM) constitutes a promising method for multiunit recordings with millisecond resolution in biological tissues.

Keywords: Two-photon scanning microscopy (TPSM); Random-access two-photon scanning microscopy (RA-TPSM); Ultrafast scanning; Acousto-optical deflectors (AODs); Temporal pre-compensation; Spatial pre-compensation; Calcium imaging; Multiunit recording

1. Introduction

In two-photon scanning microscopes (TPSM), high optical resolution of a thick scattering fluorescently labeled sample is achieved through the use of non-linear two-photon absorption from an infrared femtosecond pulsed laser (Denk et al., 1995; Zipfel et al., 2003). As the probability of a two-photon transition is a square function of photon density, excitation and fluorescent emission occur only in a small volume at the focus of a high numerical aperture objective. The emitted light is measured by a photosensitive device without descanning. Scanning the laser beam in two orthogonal in-plane directions X and Y provides an optical section of the fluorescence intensity distribution. Images result from the subsequent spatial reconstruction of the distribution in time of the fluorescence intensity. Fluorescently labeled neurons can be imaged by this method in acute brain slices and in living animals (Denk et al., 1995; Yuste et al., 2000; Helmchen and Denk, 2002; Helmchen and Waters, 2002). Scanning relies on galvanometric mirrors providing accurate scans of large amplitude, but frames are acquired at a few Hz and usually need to be averaged to get images with a useful signal to noise ratio: each point of a frame (500×500 pixels) acquired at 1 Hz is illuminated only 4 μs. Video-rate scanning is possible with a resonant galvanometer (Tsien and Bacskai, 1995; Fan et al., 1999), but again averaging of frames is usually necessary. Other promising possibilities are multifocal imaging (Straub et al., 2000) and scanning-less microscopy using temporal focusing (Oron et al., 2005), but the collection of scattered photons on an image detector results in a

* Corresponding author. Tel.: +33 1 44 32 37 34; fax: +33 1 44 32 38 87.
E-mail address: laurent.bourdieu@ens.fr (L. Bourdieu).
[1] These authors contributed equally to this work.

0165-0270/$ – see front matter © 2005 Elsevier B.V. All rights reserved.
doi:10.1016/j.jneumeth.2005.12.010

loss of spatial resolution. Finally, single line scan (Denk et al., 1995) is the most convenient method to follow physiological processes on timescales of few milliseconds, but limits the observation to biological objects transected by the same single line.

In principle, the optical measurement of time-dependent processes would not involve making images at all. Measurements are only of interest at the few locations where the image plane intersects the biological objects of interest and where maximum time should be spent to collect as many photons as possible. Fast physiological processes like action-potential-evoked calcium transients in the somata of multiple neurons or calcium entries in many neuritic compartments of a single neuron could be recorded optimally with only tens of points scattered in the field of view, each one being sampled at 1 kHz. This cannot be achieved with standard galvanometers since about 1 ms is required to stabilize them in a new position. Scanning a set of points within a plane at high speed is possible with two orthogonal acousto-optic deflectors (AODs). In an AOD, a propagating ultrasonic wave establishes a grating that diffracts a laser beam at a precise angle which can be changed within a few microseconds (Yariv, 1997). AODs have been used in a single photon microscope (Bullen et al., 1997; Bullen and Saggau, 1999). Combining scans with AODs and two-photon fluorescence excitation raises, however, some specific difficulties (Denk et al., 1995; Lechleiter et al., 2002; Iyer et al., 2003; Roorda et al., 2004). Light sources for two-photon microscopy are femtosecond pulsed lasers (∼100 fs), which have a rather large spectral dispersion $\delta\lambda$ (∼12 nm FWHM at 900 nm). The group velocity dispersion (Yariv, 1997) of the material used in an AOD therefore increases the duration of the pulse. The spatial coherence of the laser beam is also reduced since the diffraction spatially separates the wavelengths. This last feature reduces the resolution of an AOD (Iyer et al., 2003), i.e. the number of points which can be scanned. The use of AODs in TPSM is therefore not straightforward. Recently, a single axis AOD has been used to achieve ultrafast scans in one direction (Lechleiter et al., 2002; Iyer et al., 2003; Roorda et al., 2004). Setups based on a pair of highly dispersive prisms (Fork, 1984) were used to pre-compensate for the temporal broadening. The spatial dispersion introduced by the single axis AOD was also compensated, at the center of the field of view, using an additional dispersive element like a prism (Lechleiter et al., 2002; Roorda et al., 2004) or a diffraction grating (Iyer et al., 2003).

We describe the implementation of a two-dimensional AOD-based scanner in a two-photon microscope. Compensation of temporal and spatial distortions is implemented. In particular spatial compensation is obtained with an acousto-optic modulator (AOM) placed at 45° with respect to the AODs (Ngoi, 2001). Deep imaging in turbid samples with large fields of view requires the use of these pre-compensation setups that restore the microscope resolution, optimize the pulse duration at the focal point of the objective and therefore maximize the fluorescence emission. A simple model is presented, that allows quantitative analysis of temporal and spatial distortions and the future optimization of AOD-based two-photon scanning microscopes. An example of ultrafast scanning is presented, in which action-potential-evoked calcium transients in cell somata of neurons in culture are monitored.

2. Methods

2.1. All-digital two-photon microscope with galvanometric scan

Our experiments were performed on a home-made two-photon scanning upright microscope. The optical setup is shown in Fig. 1. Excitation was produced by a tunable titanium-sapphire laser (Tsunami, Spectra Physics, USA). Experiments were performed at 840 and at 900 nm. For standard two-photon imaging, the beam was scanned with a pair of galvanometric mirrors imaged on the rear pupil of the objective by an afocal telescope T_2 (magnification $T_2 = 3$). We used a resonant scanner (8 kHz CRS, GSI Luminosics, Germany) in the *X*-direction and a closed-loop scanner (M2ST with Minisax driver board, GSI Luminosics, Germany) for the *Y*-direction, so that video rate scanning was obtained. Most of the experiments were performed with the Zeiss IR-Achroplan 40× water immersion objective (numerical aperture (NA) 0.8), which has a focal length of $f_{obj} = 4.125$ mm. With this objective, the galvanometric scanners provided a field of view of 220 μm. We also used, when specified, the Olympus XLUMPlanFl 20×, NA 0.95, water immersion objective ($f_{obj} = 9$ mm) and the Zeiss Plan Neofluar 63×, NA 1.25, oil immersion objective ($f_{obj} = 2.62$ mm). The epifluorescence was collected onto a photon-counting photomultiplier (Hamamatsu, H7421-40) by imaging with an aspheric lens the objective rear pupil on the photodetector (Fig. 1). Photon

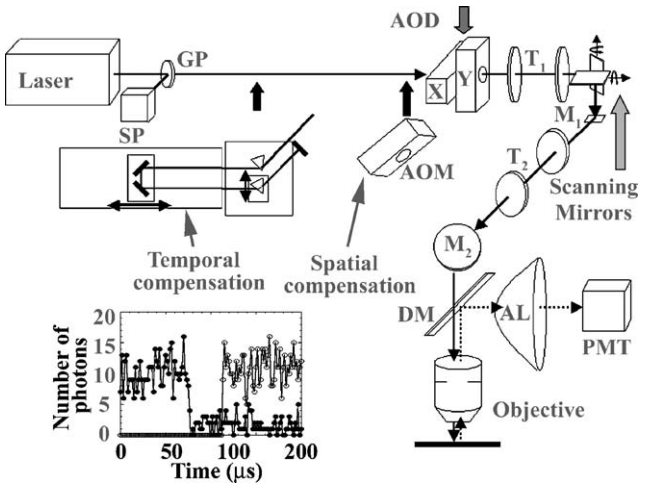

Fig. 1. Setup of the digital two-photon scanning microscope. The two scanning systems (acousto-optic deflectors and galvanometers) are shown as well as the temporal (a pair of prisms) and spatial (AOM at 45° with respect to the AODs axis) pre-compensation setups. GP, glass plate; SP, spectrometer; AOD, acousto-optic deflectors; AOM, acousto-optic modulator; T_1 and T_2, afocal telescopes (magnifications $T_1 = 1$, $T_2 = 3$); scanning mirrors, mirrors on galvanometers; M_1 and M_2, mirrors; DM, dichroic mirror; AL, aspheric lens; PMT, photomultiplier tube. *Inset:* Measure of the commutation time of the acousto-optic deflector between two angles (●) and two amplitudes (◯). The acquisition time is 1.67 μs.

counting mode (Wier et al., 2000) allows a higher signal to noise ratio at low fluorescence levels, and thus a weaker illumination, reducing photo-damage. The objective was mounted on a motorized translation stage (426, actuator VP25AA, ESP300 controller, accuracy 0.1 μm, Newport, USA) to achieve 3D scanning. We developed acquisition software with Labview (National Instruments, USA). Scanners were controlled with a multifunction digital/analog board (National Instruments, PCI-16E4). Image acquisition was performed in an all-digital mode, by counting the TTL pulses provided by the photo-multiplier with a DSP board (ADR128-C6X, Ateme, France), which had a configurable internal clock up to 10 MHz.

2.2. Acousto-optic deflectors

An acousto-optic deflection system composed of two AODs crossed at 90° (DTS-XY-250, A&A, France) was inserted into our two-photon microscope (Fig. 1). AODs were made of TeO_2 used in slow-shear acoustic wave mode (acoustic velocity $v = 650$ m/s). Two different AOD scanners were used in this paper. Experiments without spatial pre-compensation were performed with a scanner optimized at 900 nm, with a central frequency $F_0 = 80$ MHz. Experiments with spatial compensation were achieved with a scanner optimized at 840 nm with a central frequency $F_0 = 100$ MHz; an additional AOM was added to these two AODs for spatial pre-compensation (see below). Besides the difference in the central frequency and in the optimum wavelength, both scanners were identical (material, aperture, thickness) and could be used over a range of wavelengths (at least ±70 nm) as required for broadband lasers. The AODs were imaged onto the scanning mirrors by a second afocal telescope T_1 (magnification $T_1 = 1$) and on the objective rear pupil with a total magnification $T = T_1 \cdot T_2 = 3$. We used a collimated beam at the AODs with a diameter $D_{\mathrm{AOD}}^{\mathrm{beam}}$ (measured at $1/e^2$) of about 1.5–2 mm, smaller than the optical aperture of each AOD (4.2 mm). This allows maximum transmission in intensity and a very fast commutation time t_c, since this varies linearly with the beam diameter (see below). The magnification T was chosen to significantly underfill the rear pupil of the 40× objective (diameter 6.6 mm) and to obtain an effective numerical aperture of about 0.5–0.6. Deep imaging in scattering tissue is indeed theoretically more easily achieved with NA slightly lower than 0.7 (Dunn et al., 2000), because oblique rays traveling a longer path are strongly scattered. Experimentally, NA as low as 0.5 have been used at large depths of imaging (Theer et al., 2003).

We measured a large transmission (>60%) of the AODs (A&A specification: at least 70% per AOD and 50% for two AODs). Such transmission was measured over a frequency range ΔF of 30–35 MHz, depending on the fine alignment of the AODs. Within this acousto-optic bandwidth, the transmission varied by less than 10% with a shape characteristic of the anisotropic interaction in shear mode. The field of view corresponding to this bandwidth can be calculated as follows. For an AOD in the Bragg configuration, the relationship between the diffraction angle $\theta(\lambda)$ of the incident light of wavelength λ and the ultrasonic frequency F is given, by (Yariv, 1997):

$$\theta = \frac{\lambda F}{v} \tag{1}$$

where v is the sound velocity. The maximum scan amplitude $\Delta\theta_{\max}$ is proportional to the acoustic bandwidth ΔF:

$$\Delta\theta_{\max} = \frac{\lambda \Delta F}{v} \sim 44\ \mathrm{mrad} = 2.5^\circ \tag{2}$$

This amplitude is intermediate between the large angular deflection of galvanometric mirrors and the scanning range of acousto-optic deflectors in longitudinal mode or of standard piezoelectric mirrors. The field of view (FOV) obtained in the object plane depends on the magnification T of the telescope used to image the AODs onto the objective rear pupil:

$$\mathrm{FOV} = \frac{f_{\mathrm{obj}} \Delta\theta_{\max}}{T} \sim 60\ \mathrm{mm} \tag{3}$$

The angles of deviation corresponding to the in-plane directions X and Y are defined by the frequencies F_X and F_Y of the ultrasonic waves in each AOD. Both frequencies are controlled digitally with a fast output board (NI, PCI-DIO-32HS). The intensity of the diffracted beam was controlled by changing the amplitude of the ultrasonic waves. To record the fluorescence in a set of user-defined (in number and position) points, we used a counter acquisition board (NI, PCI-6602) synchronized with the digital board. For each point, the illumination was controlled in duration (from 10 μs up to seconds) as well as in intensity (to optimize in each point the signal to noise ratio while minimizing photo-bleaching and photo-damage). The software allows for standard imaging by performing TV like scans and for sampling a set of user-selected points at very high rate. We used a fast photodiode to measure the commutation times in amplitude and in frequency of the AOD. The commutation time in amplitude was measured by focusing the laser in a fluorescein solution, by switching the amplitude of the ultrasonic waves from zero to maximum and by measuring the resulting change in fluorescence. The commutation time in deflection was obtained similarly by switching the AODs between two angles of diffraction corresponding to different transmitted powers. We measured the same commutation time t_c in amplitude and in deflection of about 2.5 μs in our setup (Fig. 1 inset) as expected ($t_c = D_{\mathrm{AOD}}^{\mathrm{beam}}/v \sim 2.5$ μs).

2.3. Characterization of the temporal and spatial distortions in the acousto-optic deflectors

We characterized the time broadening of the femtosecond pulses in the AODs, that was due to the group velocity dispersion (GVD) of TeO_2. Pulse duration was measured with a home-made auto-correlator (courtesy of O. Crégut, IPCMS, Strasbourg). Pulse duration t_p was calculated from the FWHM of the auto-correlation function t_{ac} using a Gaussian shape approximation ($t_{ac} = 1.41 t_p$). A classical temporal pre-compensation system consisting of a double pass within a set of two SF10 Brewster

prisms (Fork, 1984) was inserted in the optical setup to introduce a controlled amount of negative linear chirp. The negative GVD introduced by this setup (GVD_{prisms}) was estimated by measuring the time broadening of the pulses for several inter-prisms distances ($GVD_{prisms} = -100 \pm 15\ fs^2/cm$). We used the two-photon-excited fluorescence from an FITC solution to adjust the inter-prism distance which compensated for the GVD of the whole optical setup including the objective, in order to obtain an optimum pulse duration in the sample.

The spatial distortion of the laser pulse in the AODs was characterized by measuring its effect on the radial and axial resolutions of the microscope (see below). Pre-compensation of this spatial distortion was achieved with an acousto-optic modulator (AA.MTS.141, A&A). The AOM was placed at 45° with respect to the axis of the AOD. It was carefully aligned to maximize its transmission (>80%). The frequency in the AOM was optimized experimentally to obtain a perfect spatial compensation at the center of the field of view and minimal distortions on its edge.

2.4. Resolution of the microscope

Images of sub-resolution beads, obtained with the AODs, gave access to the radial resolution of the microscope, defined as the full width at half maximum (FWHM) of the fluorescence intensity profile. The radial resolution was measured for beads at different positions in the field of view and, by this means, as a function of the ultrasonic frequencies in the AODs. The same result was obtained by acquiring images with the galvanometers for different fixed frequencies in the AODs. A stack of images at different axial positions Z (step of 0.5 μm) gave access to the axial resolution. At each Z, the maximum intensity was determined and the axial intensity profile deduced. A Gaussian expression was fitted to radial and axial intensity profiles to determine the radial and axial resolutions.

2.5. Characterization of the two-photon fluorescence excitation

We checked how the two-photon fluorescence excitation was modified by the AODs, as a function of the depth of imaging in a turbid sample. We compared, using pulses of the same duration and power at the sample, the decrease of the fluorescence intensity with the AODs and without the AODs on the optical path as a function of the depth of imaging in a homogeneous solution of latex beads (1 μm diameter, 2.5% in volume in H_2O/D_2O), in which fluorescein was added at a concentration of 1 mM. The scattering length of the suspension was of the order of 100 μm at 900 nm.

2.6. Calcium imaging of cell cultures

Pyramidal neurons from rat hippocampus were grown on glass substrates according to a protocol derived from Banker (Goslin and Banker, 1991) described in detail elsewhere (Wyart et al., 2002). Cultures were loaded with 2.5 μM of the membrane-permeant acetoxymethyl ester of Oregon-Green Bapta-1 (Molecular Probes, $K_d \sim 170$ nM) for 20 min at room temperature and rinsed for 10 min. Individual action potentials gave about 5% of fluorescence variation (Smetters et al., 1999; Peterlin et al., 2000). Experiments were performed at 900 nm with an incident power of 5 mW.

3. Results

3.1. Temporal distortion of the laser pulses in the AODs and its pre-compensation

3.1.1. Background

Due to its high acousto-optic figure of merit, the slow-shear acoustic wave mode of our AODs offers a much higher diffraction efficiency and a larger acousto-optic bandwidth than the longitudinal mode (Iyer et al., 2003). Since two AODs are required for scanning an image and since power limits the imaging depth in turbid samples, slow-shear mode TeO_2 AODs are required in two-photon microscopy. However, when ultrashort pulses travel a length L through a highly dispersive material such as TeO_2 of index of refraction $n(\omega)$, their duration is increased since each spectral component ω accumulates different amounts of phase $\phi(\omega) = n(\omega)L\omega/c$. The broadening is related to the group delay dispersion (GDD, unit of fs^2), which is the second derivative of the phase with respect to the frequency ($GDD = \phi''(\omega)$). The material is characterized by the group delay dispersion per unit of length, the group velocity dispersion ($GVD = \phi''(\omega)/L$, unit of fs^2/cm), which is related to the first and second derivatives of its index of refraction as:

$$\mathrm{GVD}(\omega) = 2n'\frac{(\omega)}{c} + \omega n''\frac{(\omega)}{c} = \left(\frac{\lambda^3}{2\pi c^2}\right) n''(\lambda) \tag{4}$$

As a consequence, a transform-limited laser pulse with a Gaussian envelope and of initial duration t_{in} is broadened, by a dispersive element of total group delay dispersion $L{\cdot}GVD$, to a final duration t_{out}, given by:

$$t_{out} = t_{in} \cdot \sqrt{1 + \left(\frac{4\ \ln 2 \cdot L \cdot \mathrm{GVD}}{t_{in}^2}\right)^2} \tag{5}$$

3.1.2. Pulse broadening and GDD of the AODs

We measured the temporal auto-correlation function of the laser beam at different points in the microscope, in particular before and after the AODs. The shorter the wavelength, the larger the time broadening expected, since the GVD decreases for increasing wavelengths. Experiments were therefore performed at 840 nm, with a pulse width of 9 ± 0.5 nm. Assuming a Gaussian envelope for the pulse (i.e. the product of the pulse duration (FWHM) by its frequency width (FWHM), the time bandwidth product (TBP), is equal to 0.441), it corresponded to a pulse duration in the oscillator of 115 ± 8 fs (Fig. 2A). The auto-correlation function just before the AODs had a FWHM of 184 ± 15 fs corresponding for a Gaussian envelope to a time duration of 130 ± 10 fs (Fig. 2A). This slight increase (to a TBP of 0.5) might be due to the GVD encountered on the beam path and to some amount of uncompensated GVD in the cavity. Pulse duration after the AODs increased markedly

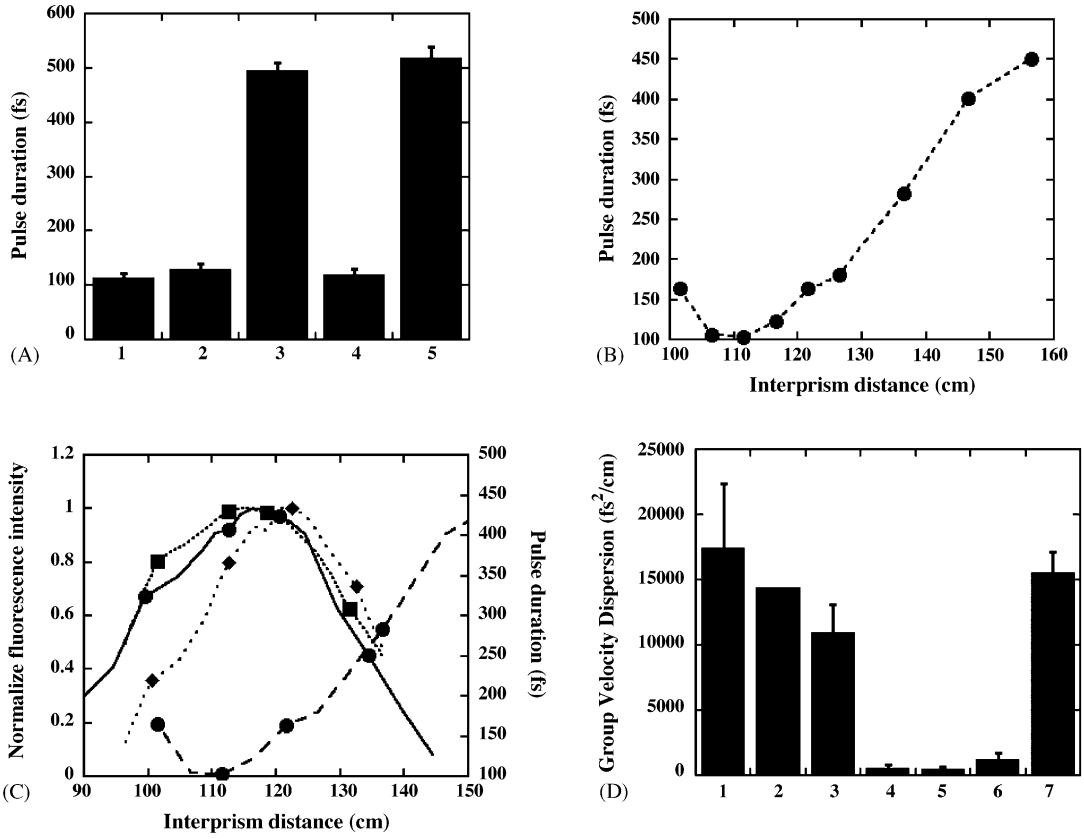

Fig. 2. Temporal dispersion of the laser pulses and its pre-compensation. All experiments were performed at 840 nm with a pulse width of 9 nm. (A) Laser pulse duration (FWHM) at different positions: (1) theoretical value in the laser cavity for a transform-limited pulse with a Gaussian envelope; (2) measured at the exit of the laser; (3) measured after the AODs; (4) measured after the AODs and with temporal pre-compensation; (5) estimation of the pulse duration at the focus of the 40× objective without any temporal pre-compensation. (B) Pre-compensation of the laser pulse broadening in the AODs. (C) Pre-compensation of the laser pulse broadening in the microscope for the Olympus XLUMPlanFl 20× objective ((■) and dotted line) and the Zeiss IR-Achroplan 40× objective ((●) and solid line) and the Zeiss Plan 63× objective objective ((♦) and dotted line). The dashed line indicates the pulse duration as a function of the inter-prism distance after the AODs (B). (D) Group velocity dispersion: (1) of the AODs estimated from the pulse temporal broadening; (2) of the AODs calculated from the AOD optical characteristics; (3) of the AODs estimated from the temporal pre-compensation curve (B); (4) of the Zeiss IR-Achroplan 40× objective; (5) of the Olympus XLUMPlanFl 20× objective; (6) of the Zeiss Plan 63× objective; (7) of the whole microscope.

to 495 ± 15 fs (Fig. 2A). Using Eq. (5), we can estimate the GDD in the AODs responsible for this large time broadening: 17,500 ± 4900 fs² (Fig. 2D). We can compare this value to the expected one knowing the physical size and the acousto-optic characteristics of our AODs and the GVD of TeO_2. TeO_2 has an ordinary (n_o) and an extraordinary (n_e) index of refraction. The value of the latter one depends on the angle of incidence with respect to the crystal optical axis. The GVD for each index of refraction can be computed using Eq. (4) and using the Sellmeir equation at the incidence used in the AODs (A&A, personal communication):

$$n_o^2 = \frac{1 + 3.7088\lambda^2}{\lambda^2 - 0.038575}; \quad n_e^2 = \frac{1 + 3.7302\lambda^2}{\lambda^2 - 0.037667} \tag{6}$$

We obtained the GVD along the ordinary axis of 4720, 4320 and 3800 fs²/cm and along the extraordinary axis of 4840, 4430 and 3890 fs²/cm at 840, 900 and 1000 nm, respectively. The laser pulse in each AOD typically travels 4 mm along the extraordinary axis, is diffracted and finally travels 11 mm along the ordinary axis. Therefore, the GDD is of the order of 14,300 fs² (Fig. 2D), in agreement with that estimated above. It is much larger than the GDD of a TPSM (a few 100 to a few 1000 fs²) (Soeller and Cannell, 1996; Muller et al., 1998).

3.1.3. Pre-compensation of pulse broadening

An optical setup has to be inserted into the optical path to provide negative GDD equal in absolute value to the positive GDD of the whole microscope including the AODs. Negative GDD can be obtained from devices providing angular dispersion, such as prisms, gratings, deformable mirrors or from dielectric mirrors with negative chirp. We used a standard pre-compensation setup consisting of a double pass through a pair of prisms (Fork, 1984). It provides an amount of negative group delay dispersion proportional to the inter-prism distance L_p and can thus be finely tuned:

$$\mathrm{GDD}_{\mathrm{prisms}} = -\left(\frac{2\lambda^3}{\pi c^2}\right) L_p n_p'^2(\lambda) \tag{7}$$

where n_p is the index of refraction of the prisms. It was possible to adjust the inter-prism distance so that the pulse duration

showed a marked minimum. At the minimum, the duration of the pulses after the AODs was 120 ± 10 fs for an inter-prism distance of 110 ± 5 cm (Fig. 2B) (TBP = 0.459, very close from a Gaussian transform-limited pulse). It is possible to compensate by this method for the positive chirp introduced by the AODs. The large inter-prism distance fits easily on a standard optical table (the size of the pre-compensation setup is about half the inter-prism distance, i.e. a few tens of centimeters). Finally, knowing the negative GVD introduced by our setup (100 ± 15 fs^2/cm, see Section 2), we can get a third estimate of the positive GDD introduced by the AODs, of the order $11{,}000 \pm 2200$ fs^2 (see Fig. 2D), in acceptable agreement with the two previous estimates.

It is also possible to evaluate if third order dispersion (TOD) might play a role in pulse temporal distortion. The TOD is the third derivative of the phase ($\phi'''(\omega)$, unit of fs^3). The temporal shape of pulses after the AODs, either without or with temporal compensation did not exhibit the typical asymmetric shape linked to TOD; after temporal pre-compensation, the TBP was also very close to that of a Gaussian transform-limited pulse. The value of the TOD in the AODs can be computed from Eq. (6) and from the definition of the TOD:

$$\mathrm{TOD} = \phi'''(\omega) = -\left(\frac{\lambda^4}{4\pi^2 c^3}\right)(3n''(\lambda) + \lambda n'''(\lambda)) \tag{8}$$

Using this equation, the TOD in the AODs is of the order of 8700 fs^3. The TOD is a third order correction of the phase accumulation when the pulse (duration Δt) travels through a dispersive medium. Its contribution, which scales as TOD/Δt^3, is only about 0.5% of the contribution of the GDD, which scales as GDD/Δt^2, and can be neglected. It seems therefore not necessary to envisage the use of an additional setup for TOD compensation.

To compensate for the GDD of the rest of the microscope including the objective, we used the fluorescence signal from a concentrated solution of fluorescein as a temporal auto-correlation measurement for a delay equal to zero. For each objective used (see Fig. 2C), the inter-prism distance was increased appropriately with respect to the position used with the AODs. We found that this adjustment could significantly increase the amount of fluorescence collected. From the positions of the prisms, we estimated the GDD of each objective. Whereas the GDD for the Zeiss 40× and the Olympus 20× objectives were rather low, a few 100 fs^2/cm, the Zeiss 63× objective introduced significantly more GDD (Fig. 2D), as expected for an objective including more corrections of aberrations and in agreement with previous auto-correlation measurements (Muller et al., 1998). Finally, without temporal pre-compensation, pulses would have been broadened to 520 fs by the AODs and the 40× objective (Fig. 2A).

The fact that ultrashort laser pulses are broadened in duration by a large numerical factor (∼4–5) in the AODs is a major limitation for in vivo imaging, since the fluorescence emission rates F scales as (Oheim et al., 2001):

$$F \propto \frac{P_0^2}{f\tau} \tag{9}$$

where f is the laser pulse rate, τ the pulse duration and P_0 is the average laser power. Therefore, the fluorescence emission is reduced by the same factor and higher laser intensities are needed. The pre-compensation setup introduces a loss in laser power of ∼20% using prisms at Brewster angle and highly reflective dielectric broadband mirrors. At low imaging depth laser power is not a limitation for imaging. The use of short pulses is still advantageous, since it allows, for a same signal to noise ratio, to reduce the heating of the tissue and the photo-bleaching. At larger depth of imaging, the available laser power limits actually the maximum depth of imaging $z_{\max}$, which scales as:

$$z_{\max} \sim l_s^{(\mathrm{ex})} \ln\left(\gamma P_0 \sqrt{\frac{1}{f\tau}}\right) \tag{10}$$

where $l_s^{(\mathrm{ex})}$ is the scattering length for the excitation light in the tissue, $\gamma = \sqrt{\eta_2 \varphi(z_{\max})/P(z_{\max})}$, η_2 the fluorescence quantum efficiency under two-photon excitation, $\phi(z)$ the fluorescence collection efficiency and $P(z)$ is the required average excitation power at the focal plane (Oheim et al., 2001; Theer et al., 2003). Therefore, despite the loss of 20% in the excitation power, it is worth using a temporal compensation setup in order to obtain pulses four to five times shorter.

3.2. A two-photon microscope based on acousto-optic deflectors without spatial pre-compensation

3.2.1. Background

The second difficulty in implementing AODs as scanners in TPSM is the spatial dispersion of the polychromatic laser pulses induced by the diffraction of light in the AODs. For a single AOD in the Bragg configuration, the diffraction angle $\theta(\lambda)$ is linked to the ultrasonic frequency F by Eq. (1) ($\theta = \lambda F/v$) and the scan amplitude $\Delta\theta_{\max}$ to the acoustic bandwidth ΔF by Eq. (2) ($\Delta\theta_{\max}(\lambda) = \lambda \Delta F/v$). The resolution of an AOD is defined as the number N of distinct spots achievable. For monochromatic light, the resolution is limited by the diameter of the beam at the AOD ($D_{\mathrm{AOD}}^{\mathrm{beam}}$), which here was smaller that the aperture of the AOD (see Section 2) and which defines the diffraction-limited angular spread $\Delta\theta_{\mathrm{diff}}$ of the laser beam after the AOD: for a TEM$_{00}$ laser beam, $\Delta\theta_{\mathrm{diff}}(\lambda) = (4/\pi)\lambda/D_{\mathrm{AOD}}^{\mathrm{beam}}$. Since in TPSM the resolution is improved by a factor $\sqrt{2}$ due to the non-linear absorption of two photons, one obtains:

$$N_{\mathrm{diff}} = \sqrt{2}\frac{\Delta\theta_{\max}(\lambda)}{\Delta\theta_{\mathrm{diff}}(\lambda)} = \sqrt{2}\left(\frac{\pi}{4}\right) D_{\mathrm{AOD}}^{\mathrm{beam}} \frac{\Delta F}{v} \tag{11}$$

In our case, $N_{\mathrm{diff}} \sim 110$. However, a femtosecond pulse of wavelength λ_0, duration $\delta\tau$ and spectral width $\delta\lambda \sim 0.441\lambda_0^2/c\delta\tau$, is diffracted at an angle θ given by Eq. (1), with an angular spread $\Delta\theta_{\mathrm{disp}}$ of the order of:

$$\Delta\theta_{\mathrm{disp}}(\delta\lambda) \sim \delta\lambda \cdot \frac{F}{v}. \tag{12}$$

For a 110 fs pulse at 900 nm ($\delta\lambda \sim 8$ nm), $\Delta\theta_{\text{disp}}$ is of the order of 1 mrad. The resolution of an AOD is in this case:

$$N(\lambda_0, \delta\lambda) = \frac{\sqrt{2}\Delta\theta_{\max}(\lambda_0)}{\sqrt{\Delta\theta^2_{\text{disp}}(\delta\lambda) + \Delta\theta^2_{\text{diff}}(\lambda_0)}} \tag{13}$$

N(900 nm, 8 nm) is ~52. Whereas the resolution of an AOD used with a monochromatic laser is only limited by the beam diameter at the AOD (and has an upper limit which is the AOD aperture), the resolution with a femtosecond pulse laser is limited mainly by the spatial dispersion of the beam in the AOD.

In the microscope, each position X in the field of view corresponds to a distinct angle θ of the AODs:

$$X = f_{\text{obj}}\frac{\theta}{T} = f_{\text{obj}}\lambda_0\frac{F}{Tv} \tag{14}$$

The spatial dispersion introduced by the AODs reduces the radial resolution w_r of the microscope, defined as the FWHM of the squared intensity point spread function (IPSF^2). It corresponds to the dimension of the image of a sub-resolution bead. In the absence of AODs, the intensity and squared intensity profiles are:

$$I(X, Y) = I_t\frac{4\ln 2}{w^2\pi}\exp\left\{-4\ln 2\left(\frac{X^2+Y^2}{w^2}\right)\right\};$$

$$I^2(X, Y) = I_t^2\left(\frac{2\ln 2}{w_r^2\pi}\right)^2\exp\left\{-4\ln 2\left(\frac{X^2+Y^2}{w_r^2}\right)\right\};$$

$$w_r = \frac{w}{\sqrt{2}} \tag{15}$$

where w is the FWHM of the intensity and I_t is the pulse total intensity. w_r is of the order of 0.5 μm. In the presence of a single AOD along X, the diffraction-limited spot is spread along X over a typical distance $\Delta X_{\text{disp}} \sim f_{\text{obj}}\Delta\theta_{\text{disp}}/T \sim f_{\text{obj}}\delta\lambda F/Tv$. This effect can be calculated exactly as follows by using a Gaussian spectral intensity profile for the pulse:

$$I(\lambda) = \frac{I_t}{\delta\lambda}\sqrt{\frac{4\ln 2}{\pi}}\exp\left\{-4\ln 2\left(\frac{\lambda-\lambda_0}{\delta\lambda}\right)^2\right\} \tag{16}$$

Each wavelength λ of intensity $I(\lambda)\mathrm{d}\lambda$ is focused as a diffraction-limited spot centered on a position $X(\lambda)$ given by:

$$X(\lambda) - X(\lambda_0) = \frac{Ff_{\text{obj}}}{vT}(\lambda - \lambda_0) \tag{17}$$

and whose spatial distribution of intensity $I_{1\text{AOD}}(X, \lambda, \delta\lambda)$ can be computed using Eqs. (16) and (17):

$$I_{1\text{AOD}}(X, \lambda, \delta\lambda) = I(\lambda)\,\mathrm{d}\lambda\sqrt{\frac{4\ln 2}{\pi w^2}} \times \exp\left\{-4\ln 2\left(\frac{X - X(\lambda)}{w}\right)^2\right\} = I_t\frac{4\ln 2}{\pi\delta\lambda w} \times \exp\left\{-4\ln 2\left[\left(\frac{X-X(\lambda)}{w}\right)^2 + \left(\frac{\lambda-\lambda_0}{\delta\lambda}\right)^2\right]\right\} \tag{18}$$

Integrating Eq. (18) over λ, one obtains the intensity profile $I^{\lambda_0}_{1\text{AOD}}(X, \delta\lambda)$ corresponding to the summation of all the diffraction-limited spots due to each wavelength of the femtosecond pulse:

$$I^{\lambda_0}_{1\text{AOD}}(X, \delta\lambda) = I_t\sqrt{\frac{4\ln 2}{\pi(w^2 + (Ff_{\text{obj}}\delta\lambda/vT)^2)}} \times \exp\left\{-4\ln 2\frac{(X - X(\lambda_0))^2}{w^2 + (Ff_{\text{obj}}\delta\lambda/vT)^2}\right\} \tag{19}$$

The resolution of the microscope is obtained from the function ${I^{\lambda_0}_{1\text{AOD}}}^2(X, \delta\lambda)$. The image of a sub-resolution bead will therefore be an ellipse stretched along the X direction, with its small axis $w^{\text{s}}_{1\text{AOD}}$and its long axis $w^{\text{l}}_{1\text{AOD}}$ given by:

$$w^{\text{s}}_{1\text{AOD}} = w_r \quad \text{and} \quad w^{\text{l}}_{1\text{AOD}} = \sqrt{w_r^2 + \frac{1}{2}\left(\frac{\delta\lambda F f_{\text{obj}}}{vT}\right)^2} = \sqrt{w_r^2 + \frac{1}{2}\left(\frac{\delta\lambda(x+x_0)}{\lambda}\right)^2} \tag{20}$$

where $x = \lambda(F - F_0)f_{\text{obj}}/vT$ is the point in the field of view corresponding to the frequency F in the AOD ($x = 0$ at the center of the field of view), F_0 is the central frequency of the acousto-optic bandwidth and $x_0 = \lambda F_0 f_{\text{obj}}/vT$.

The fluorescence intensity is proportional to the squared intensity ${I^{\lambda_0}_{1\text{AOD}}}^2(X, \delta\lambda)$ and inversely proportional to the pulse duration (Eq. (9)). The spatial separation of the wavelengths at the objective focal plane corresponds to a spectral narrowing at any given point. In the temporal domain, it corresponds to an increase of the pulse duration, and to a smaller fluorescence yield. Using Eqs. (17), (18) and (20), the narrower spectral width of the pulse $\delta\lambda_{1\text{AOD}}$ and its longer duration $\delta t_{1\text{AOD}}$ (with respect to the duration δt when all the wavelengths are spatially superposed) can be computed:

$$\delta\lambda_{1\text{AOD}} = \left(\frac{w_r}{w^{\text{l}}_{1\text{AOD}}}\right)\delta\lambda \tag{21}$$

$$\delta t_{1\text{AOD}} = \left(\frac{w^{\text{l}}_{1\text{AOD}}}{w_r}\right)\delta t \tag{22}$$

Taking into account both the spatial and the temporal distortions, the loss of fluorescence can be computed for an object whose dimension L is (i) larger than the laser beam waist as $\frac{I^F_{1\text{AOD}}(\delta\lambda)}{I^F_{1\text{AOD}}(0)} = \frac{\int \mathrm{d}X I^2_{1\text{AOD}}(X,\delta\lambda)}{\int \mathrm{d}X I^2_{1\text{AOD}}(X,0)}\frac{\delta t}{\delta t_{1\text{AOD}}}$ and (ii) smaller than the beam waist as $\frac{I^F_{1\text{AOD}}(\delta\lambda)}{I^F_{1\text{AOD}}(0)} = \frac{I^2_{1\text{AOD}}(X(\lambda_0),\delta\lambda)}{I^2_{1\text{AOD}}(X(\lambda_0),0)}\frac{\delta t}{\delta t_{1\text{AOD}}}$:

$$\frac{I^F_{1\text{AOD}}(\delta\lambda)}{I^F_{1\text{AOD}}(0)} = \frac{w_r^2}{w_r^2 + 1/2(Ff_{\text{obj}}\delta\lambda/vT)^2} = \left(\frac{w_r}{w^{\text{l}}_{1\text{AOD}}}\right)^2, \quad \text{for } L \gg w^{\text{l}}_{1\text{AOD}} \tag{23a}$$

$$\frac{I^F_{1\mathrm{AOD}}(\delta\lambda)}{I^F_{1\mathrm{AOD}}(0)} = \frac{w_r^3}{\left(w_r^2 + 1/2(Ff_{\mathrm{obj}}\delta\lambda/vT)^2\right)^{3/2}} = \left(\frac{w_r}{w^1_{1\mathrm{AOD}}}\right)^3, \quad \text{for } L \ll w^1_{1\mathrm{AOD}} \tag{23b}$$

In our case, two crossed AODs along the orthogonal directions X and Y are used at frequencies F_X and F_Y. The IPSF^2 is then an ellipse oriented along an angle θ_{AOD}, with a small axis $w^s_{2\mathrm{AOD}}$ and a long axis $\omega^l_{2\mathrm{AOD}}$ given by:

$$\theta_{\mathrm{AOD}} = \arctan\left(\frac{F_Y}{F_X}\right), \quad w^s_{2\mathrm{AOD}} = w_r,\ w^l_{2\mathrm{AOD}} = \sqrt{w_r^2 + \frac{1}{2}\left(\frac{\delta\lambda\sqrt{F_X^2+F_Y^2}f_{\mathrm{obj}}}{vT}\right)^2} = \sqrt{w_r^2 + \frac{1}{2}\left(\frac{\delta\lambda(\sqrt{x^2+y^2}+\sqrt{x_0^2+y_0^2})}{\lambda}\right)^2} \tag{24a}$$

where $(x, y) = (\lambda(F_X - F_0)f_{\mathrm{obj}}/vT,\ \lambda(F_Y - F_0)f_{\mathrm{obj}}/vT)$ is the point corresponding to the frequencies (F_X, F_Y) ($x = y = 0$ at the center of the field of view) and $x_0 = y_0 = \lambda F_0 f_{\mathrm{obj}}/vT$. For $F = F_X = F_Y$ ($x = y$), this expression simplifies to:

$$\theta_{\mathrm{AOD}} = 45^\circ, \quad w^s_{2\mathrm{AOD}} = w_r, \quad w^l_{2\mathrm{AOD}} = \sqrt{w_r^2 + \left(\frac{\delta\lambda F f_{\mathrm{obj}}}{vT}\right)^2} = \sqrt{w_r^2 + \left(\frac{\delta\lambda(x+x_0)}{\lambda}\right)^2} \tag{24b}$$

The loss of fluorescence, for an object of dimension L, respectively, larger and smaller than the beam waist, is given by:

$$\frac{I^F_{2\mathrm{AOD}}(\delta\lambda)}{I^F_{2\mathrm{AOD}}(0)} = \frac{w_r^2}{w_r^2 + (Ff_{\mathrm{obj}}\delta\lambda/vT)^2} = \left(\frac{w_r}{w^l_{2\mathrm{AOD}}}\right)^2, \quad \text{for } L \gg w^l_{2\mathrm{AOD}} \tag{25a}$$

$$\frac{I^F_{2\mathrm{AOD}}(\delta\lambda)}{I^F_{2\mathrm{AOD}}(0)} = \frac{w_r^3}{\left(w_r^2 + (Ff_{\mathrm{obj}}\delta\lambda/vT)^2\right)^{3/2}} = \left(\frac{w_r}{w^l_{2\mathrm{AOD}}}\right)^3, \quad \text{for } L \ll w^l_{2\mathrm{AOD}} \tag{25b}$$

The spatial distortion of the laser pulse due to the AODs significantly reduces their resolution. The reduction in the AODs' resolution induces, as demonstrated by Eqs. (24a), (24b), (25a) and (25b), some important limitations on the optical resolution and of the fluorescence yield. Without pre-compensation of this spatial distortion, it is possible using Eqs. (24a), (24b), (25a) and (25b) to choose the telescope T such that the microscope resolution and the two-photon fluorescence excitation are reasonably reduced. In the following, we show that this is achieved using our experimental conditions.

3.2.2. Experimental results

Using laser pulses at 900 nm of spectral width 8 nm and with $F_0 = 80$ MHz, a sub-resolution bead is imaged according to our model as an ellipse with a long axis of 1.15 μm (for 1AOD) and 1.49 μm (for 2AODs). Images of sub-resolution fluorescent beads (diameter 20 nm) were acquired with the galvanometric scanners, while the AODs' frequencies were fixed at 80 MHz (they were not scanning). Fig. 3A shows, for comparison, the image of bead without an AOD in the optical path. It has, as expected, a radial symmetry with a FWHM of 0.65 ± 0.05 μm. In the axial direction, the resolution was 2.95 ± 0.5 μm. Those values are in good agreement with the theoretical values obtained using Zipfel et al. (Zipfel et al., 2003) for an effective numerical aperture NA ∼ 0.6: radial FWHM = $0.377\lambda/\mathrm{NA} = 0.57$ μm and axial FWHM $= 0.626\lambda/(n - \sqrt{n^2 - \mathrm{NA}^2}) = 3.9$ μm. Fig. 3B was obtained with a single axis AOD in the optical path. The image of a bead is stretched in the direction parallel to the axis of the AOD. Quantitatively, the resolution along the stretched direction decreased by a factor ∼1.5 and was equal to 1.00 μm with a single AOD. The resolution in the direction perpendicular to the AOD axis was not modified (0.65 μm). These values are in good agreement with the loss of resolution estimated using Eq. (20). Fig. 3E plots the resolution of the microscope as a function of the frequency F_X for a single AOD. The resolution perpendicular to the AOD axis was independent of the frequency. In contrast, the resolution along the AOD axis decreased with increasing frequency, in good agreement with Eq. (20) (no adjustable parameters). The resolution varied typically by 12% in the field of view (1.00 ± 0.12 μm). In presence of the two AODs (Fig. 3C), the image of a bead is stretched along an axis tilted by an angle θ_{AOD} given by Eq. (24a). In Fig. 3C, $F_X = F_Y$ and $\theta_{\mathrm{AOD}} = 45^\circ$ with respect to the deflectors' orientation. Quantitatively, the resolution decreased by a factor ∼2.2 (1.4 ± 0.14 μm) at the center of the field of view. The variation of the resolution within the field of view (along the direction $F_Y = F_X$) corresponds precisely to the theoretical curve obtained with no adjustable parameters using Eq. (24b). The long axis of the ellipse varied by ±0.2 μm in the field of view. The resolution along the perpendicular direction remained, at any frequency, equal, as expected, to the resolution of the microscope without the AODs (0.65 μm) (Fig. 3E). Fig. 3D was obtained with a laser pulse at 900 nm which was not transform-limited. It had indeed the same duration as above but a larger spectral bandwidth (17 nm instead of 8 nm). It shows that the length of the ellipse long axis was linked to the spectral width of the laser, as expected from Eq. (24b). Finally, the axial resolution was not modified by the AODs and had a typical value of 2.95 ± 0.5 μm.

We then analyzed the loss of fluorescence due to the spatial distortion. Without scanning, we focused the laser beam in a turbid FITC solution (see Section 2) and compared the fluorescence collected, with and without the AODs (Fig. 3F). We performed these measurements at the same wavelength and incident power

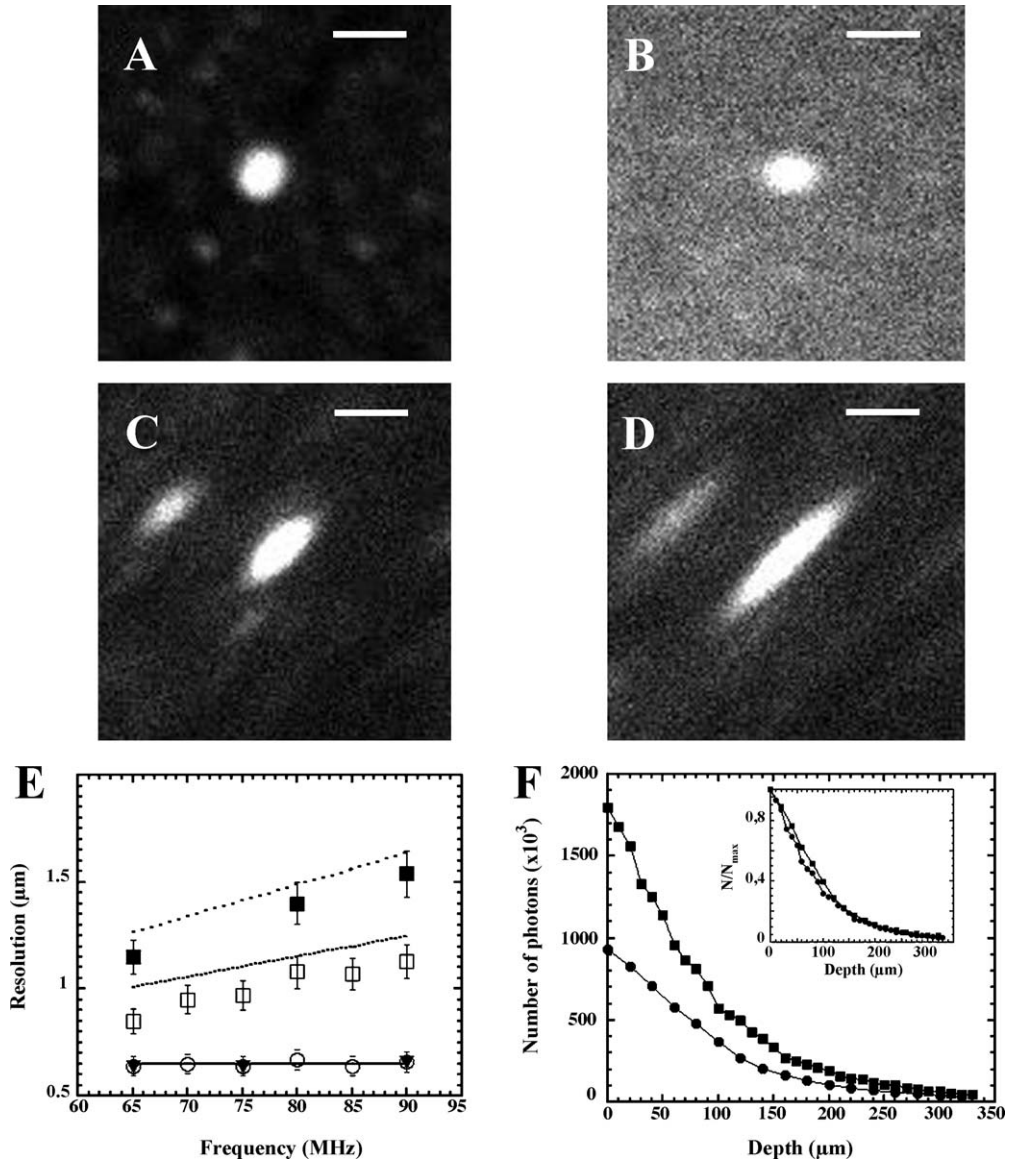

Fig. 3. Implementation of AODs without spatial compensation in a two-photon microscope. All experiments were performed at 900 nm with a pulse width of 8 nm (except when explicitly mentioned). (A–D): 10 μm × 10 μm images (sum of 100 frames obtained at video rate with the galvanometric scanners) of a 20 nm fluorescent bead. The scale bar is 2 μm: (A) without AOD on the optical path; (B) with a single AOD along the horizontal direction X ($F_X = 80$ MHz); (C) in the presence of 2AODs ($F_X = F_Y = 80$ MHz); (D) in the presence of 2AODs ($F_X = F_Y = 80$ MHz) for a pulse width of ∼17 nm; (E) radial resolution of the microscope in the presence of a single axis AOD along X as a function of the ultrasonic frequency F_X and in the presence of the 2AODs as a function of the ultrasonic frequency $F = F_X = F_Y$. (◯) 1AOD, resolution along Y. (□) 1AOD, resolution along X. (♦) 2AODs, resolution along the small axis of the ellipse (direction $F_X = -F_Y$). (■) 2AODs, resolution along the long axis of the ellipse (direction $F_X = F_Y$). Solid line: resolution without AOD: 0.65 μm. Dotted line: resolution along X for 1AOD using Eq. (20) of the text, with $\delta\lambda = 8$ nm, $w_r = 0.65$ μm and $F_0 = 80$ MHz. Dashed line: resolution along the long axis of the ellipse for 2AODs using Eq. (24b), with $\delta\lambda = 8$ nm, $w_r = 0.65$ μm and $F_0 = 80$ MHz. (F) Fluorescence intensities (at the same laser power at the back aperture of the microscope and for the optimum temporal pre-compensation) as a function of the depth in a solution of latex beads (1 μm in diameter, 2.5% in volume, in H_2O/D_2O stained with fluorescein) with the AODs (●) and without AODs (■). *Inset:* Evolution of the relative fluorescence intensities (the fluorescence intensity normalized by the fluorescence intensity at the surface of the sample), as a function of the imaging depth.

in the sample and without saturating the fluorescence emission. Pre-compensation of the temporal distortion was optimized in each case. In the presence of the AODs, the fluorescence emission was of the order of one half of the intensity observed without the AODs. Both curves were fitted to an exponential with a length scale of ∼90 μm. The difference in intensity can be attributed to the spatial distortion. The insert in Fig. 3F shows the fluorescence normalized by the one at the top of the sample. As the two curves fold together, it demonstrates that AODs reduce the depth of imaging in a turbid sample only because of the reduction in laser power and in spatial resolution. Therefore, without spatial pre-compensation, AODs can be used in TPSM, but with severe constraints on the field of view to prevent a too large loss of resolution.

3.3. A two-photon microscope based on acousto-optic deflectors with spatial pre-compensation

3.3.1. Background

An additional dispersive element must be used to suppress the angular dispersion of the wavelengths due to the AODs. As such a setup introduces a fixed amount of dispersion, it can only compensate perfectly for the distortion at the center of the field of view. It can be placed before the AODs as a spatial pre-compensation setup. Different dispersive elements have been used to compensate for the distortion introduced by only a single AOD, e.g. prisms (Lechleiter et al., 2002; Roorda et al., 2004) and gratings (Iyer et al., 2003). To compensate for the larger dispersion due to two crossed AODs, the use of an AOM as a prism with an adjustable apex angle was proposed in the field of laser metallurgy (Ngoi, 2001). We used an AOM placed at 45° with respect to the two axes of the AODs (Fig. 4A) and chose appropriately the propagation direction and the frequency of the ultrasonic wave in the AOM, which propagates in the opposite direction with respect to the sum of the two waves in the AODs (Fig. 4A). In order to compensate for the spatial distortion at the center of the field of view ($F_X = F_Y = F_0$), its frequency was fixed at a value F_{AOM} given by:

$$F_{\mathrm{AOM}} = F_0 \cdot \sqrt{2} \tag{26}$$

This solution offers the possibility to change the amount of compensation in the AOM as a function of the wavelength, to get a tunable scanner. The pre-compensation is perfect at the center of the field of view and partial at points far from the center. On the diagonal ($F_X = F_Y = F$), the resolution along the long ($w^{\mathrm{l,c}}_{\mathrm{2AOD}}$) and small ($w^{\mathrm{s,c}}_{\mathrm{2AOD}}$) axis and the loss in fluorescence ($I^{F,\mathrm{c}}_{\mathrm{2AOD}}(\delta\lambda)/I^{F,\mathrm{c}}_{\mathrm{2AOD}}(0)$) can be estimated by replacing F by $F - F_0$ ($x + x_0$ by x) in Eqs. (24a), (24b), (25a) and (25b).

$$w^{\mathrm{l,c}}_{\mathrm{2AOD}} = \sqrt{w_{\mathrm{r}}^2 + \left(\frac{\delta\lambda(F - F_0) f_{\mathrm{obj}}}{vT}\right)^2} = \sqrt{w_{\mathrm{r}}^2 + \left(\frac{\delta\lambda x}{\lambda}\right)^2}, \quad w^{\mathrm{s,c}}_{\mathrm{2AOD}} = w_{\mathrm{r}} \tag{27}$$

$$\frac{I^{F,\mathrm{c}}_{\mathrm{2AOD}}(\delta\lambda)}{I^{F,\mathrm{c}}_{\mathrm{2AOD}}(0)} = \frac{w_{\mathrm{r}}^2}{w_{\mathrm{r}}^2 + (\delta\lambda(F - F_0) f_{\mathrm{obj}}/vT)^2} = \left(\frac{w_{\mathrm{r}}}{w^{\mathrm{l,c}}_{\mathrm{2AOD}}}\right)^2, \quad \text{for } L \gg w^{\mathrm{l,c}}_{\mathrm{2AOD}} \tag{28a}$$

$$\frac{I^{F,\mathrm{c}}_{\mathrm{2AOD}}(\delta\lambda)}{I^{F,\mathrm{c}}_{\mathrm{2AOD}}(0)} = \frac{w_{\mathrm{r}}^3}{(w_{\mathrm{r}}^2 + (\delta\lambda(F - F_0) f_{\mathrm{obj}}/vT)^2)^{3/2}} = \left(\frac{w_{\mathrm{r}}}{w^{\mathrm{l,c}}_{\mathrm{2AOD}}}\right)^3, \quad \text{for } L \ll w^{\mathrm{l,c}}_{\mathrm{2AOD}} \tag{28b}$$

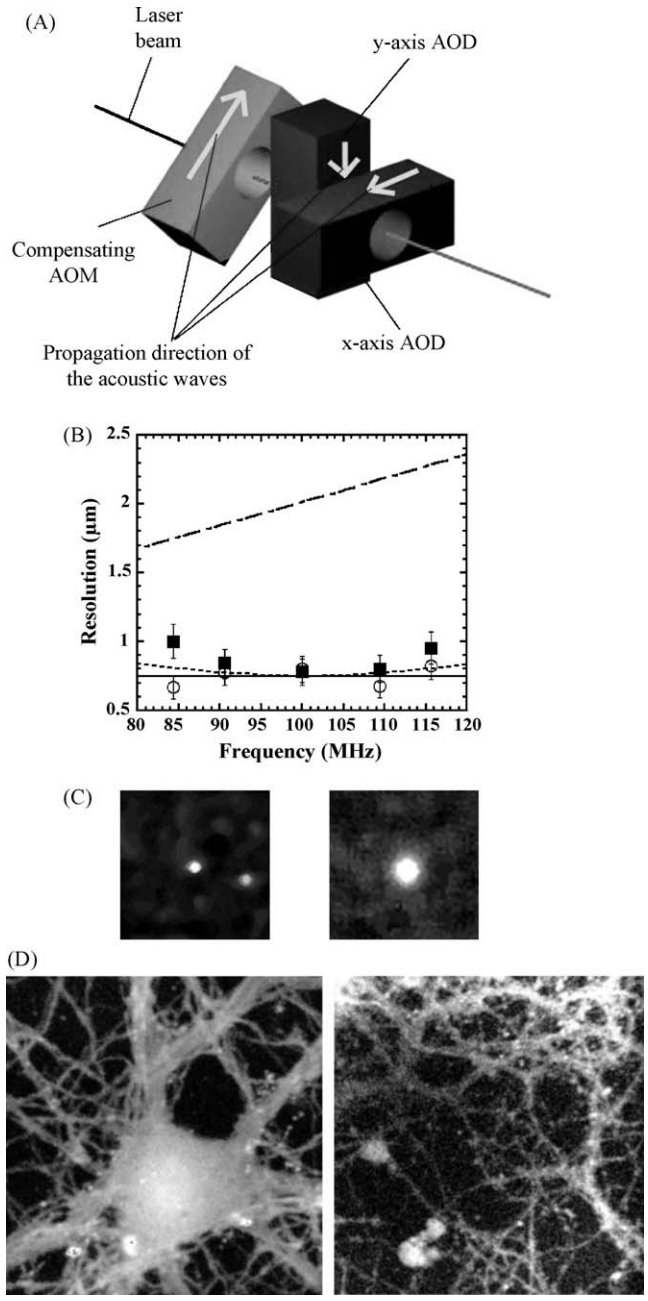

Fig. 4. The pre-compensation of the spatial distortion of the laser pulse. All the experiments were performed at 840 nm with a pulse width of 9 nm. (A) Scheme showing how the AOM was inserted at 45° before the two AODs. The propagation direction of the ultrasonic waves in each AOD is indicated by arrows. (B) Radial resolution of the microscope, after the pre-compensation of the spatial distortion, as a function of the ultrasonic frequency $F = F_X = F_Y$. Empty circle (◯): resolution along the small axis of the ellipse (direction $F_X = -F_Y$). Black square (■): resolution along the long axis of the ellipse (direction $F_X = F_Y$). Solid line: resolution without AOD (0.72 µm). Dashed line: theoretical resolution after pre-compensation using Eq. (27) of the text, with $\delta\lambda = 9$ nm and $w_{\mathrm{r}} = 0.65$ µm. Dashed-dotted line: theoretical resolution in the same configuration but without spatial pre-compensation using Eq. (24b), with $\delta\lambda = 9$ nm and $w_{\mathrm{r}} = 0.65$ µm. The axial resolution is ~2.95 µm. (C) 16 µm × 16 µm images of 20 nm in diameter fluorescent beads scanned with the AODs. *Left:* with the Zeiss 40× objective. *Right:* with the Olympus 20× objective. (D) Images of Oregon green bapta-1 AM labeled hippocampal neurons in culture scanned with the AODs. *Left:* 60 µm × 60 µm field of view obtained with the Zeiss 40× objective. *Right:* 130 µm × 130 µm field of view obtained with the Olympus 20× objective.

3.3.2. Experimental results

The resolution of the compensated microscope is shown on Fig. 4B. The resolution along the small axis was independent of the frequency as expected and was equal to $0.72 \pm 0.05\,\mu m$. It corresponds to an effective numerical aperture in this set of experiments of ~0.45. As a result of the spatial pre-compensation, the resolution along the stretched direction was close from the diffraction-limited resolution over the whole frequency range. At the center of the field of view, the spatial distortion was fully compensated, while a residual distortion was observed for points near the edge. Experimental measurements of this distortion were in excellent agreement with the theoretical curve (dashed line: Eq. (27), the distortion was 15% larger than the theoretical one). The resolution in the same conditions without spatial pre-compensation is drawn on the Fig. 4B (dashed-dotted line): the pre-compensation has improved the resolution by a factor of almost 3, and thus the two-photon fluorescence excitation by a factor 27, using Eq. (28b). Fig. 4C shows typical images of 20 nm fluorescent beads scanned with the AODs, using the 40× objective (left) and the 20× objective (right). Note in both cases the circular shape of the images of the beads, which are diffraction-limited, as compared to Fig. 3B–D. The resolution of the image with the objective 20× has only a 1 μm resolution since the effective numerical aperture for this objective in this setup was of the order of 0.3: no image could be obtained without spatial pre-compensation in this case! Images shown in Fig. 4D are scans with AODs of Oregon Green Bapta-1 AM labeled neurons in culture (see Section 2). The field of view is 60 μm (40×, left) and 130 μm (20×, right). Fine details are clearly observable. Finally, the AOM introduced the same amount of GVD as each AOD (~7000 fs^2). The total GVD of the AOM-2AODs scanner is ~21,000 fs^2 and was pre-compensated by adjusting the inter-prism distance in the temporal pre-compensation setup.

3.4. Optical recordings of action-potential-evoked calcium transients in pyramidal neuron somata

To demonstrate that recordings over a long period of time at multiple sites and at high acquisition rate can be achieved with AODs, we studied hippocampal neurons in culture. After 2 weeks in vitro, these cultures were spontaneously active (Wyart et al., 2002). To estimate optically the time of action potential

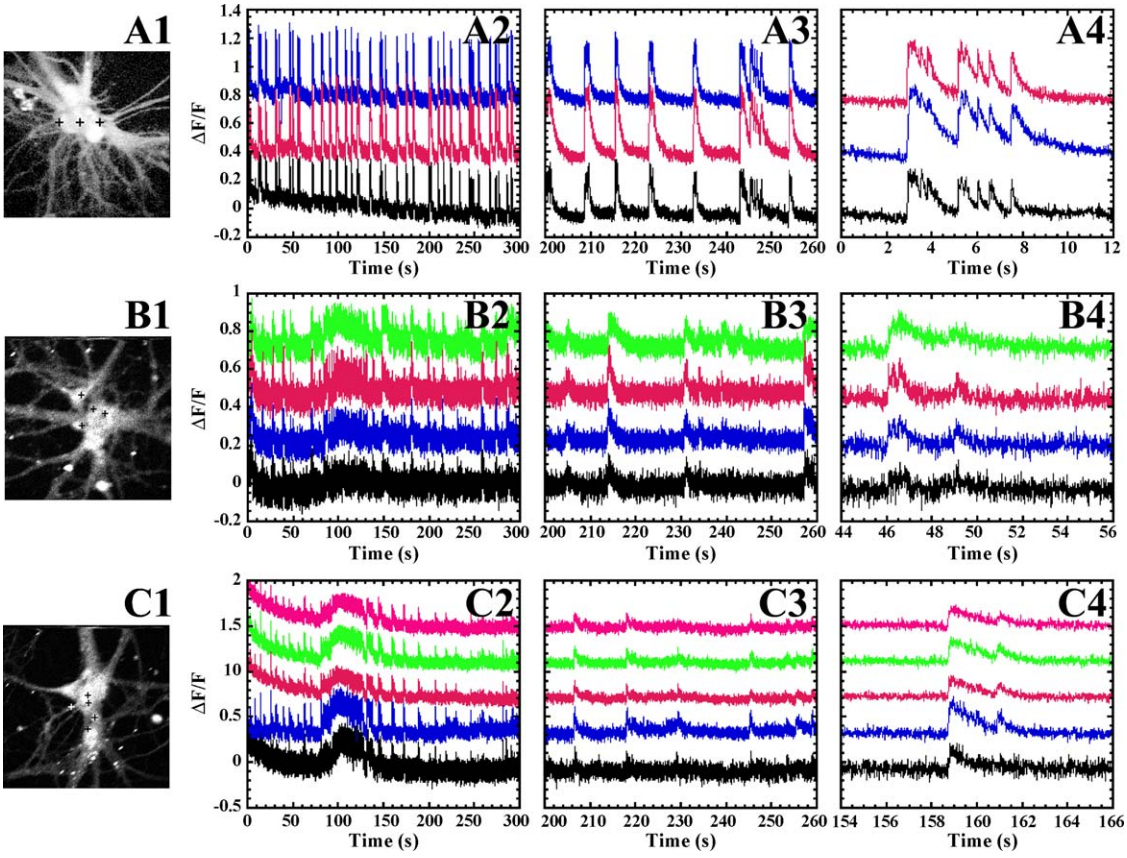

Fig. 5. Examples of ultrafast calcium imaging of spontaneous action potentials in cultured hippocampal neurons labeled with Oregon green bapta-1 AM. All experiments were performed with the Zeiss 40× objective at 900 nm with a pulse width of 10 nm; spatial compensation was not used. (A1–C1): 140 μm × 140 μm images of neurons labeled with Oregon green bapta-1 AM, obtained with the galvanometers. Points indicated by crosses on each image are scanned at a frequency of 0.1 kHz. (A2–C2) The relative variation ($\Delta F/F$) of the fluorescence intensity (F) is plotted as a function of time. (A3 and A4), (B3 and B4) and (C3 and C4) are zooms of, respectively, (A2), (B2) and (C2). Long recordings are very stable whereas zooms indicated that bursts of action potentials as well individual spikes within bursts can be visualized by this type of recording.

emission in several cells, we monitored the calcium transients in their cell bodies. These somatic calcium transients measured with high affinity dyes have a time to peak of 5–50 ms following the action potential and a relaxation time of 1–5 s (Smetters et al., 1999). We scanned three to five neurons with the AODs (Fig. 5). It shows that calcium transients can be detected simultaneously in each cell. The calcium transients had a time to peak of typically 10–15 ms in most cases and a decay time of about 1–2 s, as expected. Taking into account this time to peak of the transients, we choose a sampling rate of 0.1 kHz (even though much higher rate can be used in our setup) in order to follow the transients in each neuron with a maximum signal to noise ratio. Each neuron was therefore illuminated for a time depending on the number of scanned neurons for 10/3 = 3.3 ms (Fig. 5A2–A4), 10/4 = 2.5 ms (Fig. 5B2–B4) and 10/5 = 2 ms (Fig. 5B2–B4). Less than 5 μs was necessary to move between each point and the amount of light lost during the move was negligible (typically 5 μs/2 ms = 0.25%).

Measurements could be achieved over a long period of time, which is a striking feature (Fig. 5A2, B2 and C2). The optical recordings lasted for minutes (5 min in the cases shown) with almost no photo-bleaching in certain cases (Fig. 5A2 and C2), despite the fact that the laser was focused at each recording point for a third of the total time, i.e. a few millisecond. Therefore, very long recordings without major cell damage were possible, even though the beam was not continuously scanned at different locations, as in standard imaging. The possibility to scan a few points is therefore demonstrated. Moreover, using the AODs also as modulators, it was possible to adjust the laser power independently for each point to optimize the photon count rate and to reduce photo-toxicity. In our experiments, an average photon count rate of 500 kHz–1 MHz was used for each cell when the laser was focused on the cell body. The typical count per neuron and per time step (2–3.3 ms) was of the order of 1000–3000, respectively. The photon noise was of $\sqrt{1000} = 33$ to $\sim \sqrt{3000} = 55$ and corresponded to 3.3–2% of the signal. Successive bursts of activity consisting of series of transients separated by a few hundred milliseconds were observed in all recordings. A signal variation of 5–10% per transient was measured, which was larger than the experimental noise. The high acquisition rate enabled the observation that most of the transients are highly synchronous between the neurons.

4. Discussion

It has been believed for a long time that AODs could not be used in TPSM. The main concerns were the angular spread of the pulsed laser after an AOD and the increase of the pulse duration. Recent studies have however shown that a single AOD could be introduced into a two-photon scanning microscope to perform fast scanning in one direction. The temporal dispersion due to the single axis AOD was compensated using a double pass through a pair of prisms (Lechleiter et al., 2002; Iyer et al., 2003; Roorda et al., 2004). The spatial dispersion of the AOD was compensated using an SF11 prism (Lechleiter et al., 2002), an SF10 prism (Roorda et al., 2004) or a diffraction grating (Iyer et al., 2003). In this paper, we extend these works to a real two-dimensional AOD-based scanner introducing much larger temporal and spatial dispersions. Whereas temporal compensation of the GDD was also obtained using pairs of prisms, the spatial dispersion was compensated using an AOM placed at 45° with respect to the AODs. This latter solution allows fine tuning of the spatial compensation and the design of a wavelength tunable scanner. This paper describes for the first time a two-dimensional AOD-based scanner with compensation of both spatial and temporal distortions. Its performances are strongly supported by a simple model, which facilitates the future design of two-photon AOD-scanning microscopes fitted to the user's need in term of spatial resolution, field of view or depth of penetration.

The angular spread after the AODs dramatically decreases their resolution and strongly limits the field of view. For an uncompensated microscope, the maximum field of view $\mathrm{FOV}_{\max}$ using Eqs. (24a), (24b), (25a) and (25b) is:

$$w^1_{2\mathrm{AOD}} = \gamma w_\mathrm{r}, \quad \frac{I^F_{2\mathrm{AOD}}(\delta\lambda)}{I^F_{2\mathrm{AOD}}(0)} = \frac{1}{\gamma^2}(L > w^1_{2\mathrm{AOD}}) \quad \text{or}$$

$$\frac{I^F_{2\mathrm{AOD}}(\delta\lambda)}{I^F_{2\mathrm{AOD}}(0)} = \frac{1}{\gamma^3}(L < w^1_{2\mathrm{AOD}}) \Leftrightarrow \mathrm{FOV}_{\max} = \sqrt{\gamma^2 - 1}\, w_\mathrm{r} \frac{\lambda}{\delta\lambda} \frac{\Delta F}{F_0 + \Delta F/2} \tag{29}$$

For $\gamma = 2$, this corresponds to a $\mathrm{FOV}_{\max}$ of 45 μm (w_r = 0.65 nm, $\delta\lambda = 8$ nm, $\lambda = 900$ nm, $\Delta F = 35$ MHz, $F_0 = 80$ MHz). Larger values of γ are not acceptable in most cases. This is the simple way to implement AOD-based scanners in two-photon microscopy, but it may only be useful for in vitro studies requiring reduced fields of view. Deep imaging requires the compensation of the large spatial distortion for optimal fluorescence excitation. We have presented in this paper a technical solution based on an AOM to fully compensate at the center of the field of view for the spatial distortion introduced by a pair of AODs. At the center of the field of view, it provides, by the proper adjustment of the frequency in the AOM, a perfect correction to the loss of resolution and of fluorescence yield. This latter effect arises both from a spatial effect (restored diffraction-limited focusing) and from a temporal effect (restored optimal temporal pulse shape). The overall transmission of an AOM-AODs scanner is about 40–50%. Therefore, using a commercial laser source, hundreds of mW are available at the objective back aperture. At low depth in scattering tissues, as in thin slices, the loss of fluorescence due to remaining spatial distortion on the edge of the field of view can be compensated by increasing the illumination intensity. At higher depth, such as in in vivo studies, when there is no more laser power available, the loss in fluorescence can be compensated by increasing the time spent in points where fluorescence is lower. Spatial pre-compensation also allows imaging wider fields of view. After compensation, the residual distortion on the edges eventually limits the maximum field of

view:

$$w_{2\mathrm{AOD}}^{\mathrm{l,c}} = \gamma w_{\mathrm{r}}, \quad \frac{I_{2\mathrm{AOD}}^{F,\mathrm{c}}(\delta\lambda)}{I_{2\mathrm{AOD}}^{F,\mathrm{c}}(0)} = \frac{1}{\gamma^2}\ (L > w_{2\mathrm{AOD}}^{\mathrm{l,c}}) \quad \text{or}$$

$$\frac{I_{2\mathrm{AOD}}^{F,\mathrm{c}}(\delta\lambda)}{I_{2\mathrm{AOD}}^{F,\mathrm{c}}(0)} = \frac{1}{\gamma^3}(L < w_{2\mathrm{AOD}}^{\mathrm{l,c}})$$

$$\Leftrightarrow \mathrm{FOV}_{\max} = 2\sqrt{\gamma^2 - 1}\, w_{\mathrm{r}} \frac{\lambda}{\delta\lambda} \tag{30}$$

For $\gamma = 2$, the maximum field of view is about 220 μm, using a telescope of magnification $T = 0.82$ ($\lambda = 840$ nm, $\delta\lambda = 9$ nm, $w_{\mathrm{r}} = 0.7$ nm). This will require large AODs with a clear aperture of 11 mm. Recent studies have shown that custom AODs of 9 mm can be provided (Iyer et al., 2003). Our supplier can also provide custom AODs with apertures up to 13 mm. Spatial compensation using an AOM offers the possibility of imaging large fields of view, as is very often required in physiological studies. Finally, let us note that Eq. (30) shows that even larger fields of view might be obtained by the use of lasers with smaller spectral bandwidth (and longer pulses).

AODs offer the unique possibility of achieving extremely fast scanning of a set of points. The laser beam can be moved between points within 3–5 μs with our system. This could not be achieved with galvanometers which usually require 1 ms for a step. Moreover, galvanometers have some amount of positional noise, of the order of several tens of μrad, which also limits their accuracy for this type of scanning. Such positional noise does not exist in the AODs, which are therefore perfectly fitted to scanning individual points. Our software allows choosing a user-defined number of points of interest for acquisition rates up to a few kHz. The number of points is ultimately limited by two factors. The first limitation is the commutation time between two points. The use of larger AODs will increase this time to about 20 μs for a 13 mm in diameter AODs scanner, which is still very fast. The second limitation is the number of photons N collected per point of interest. As the photon noise ($N^{1/2}$) is the main noise, it defines the smallest signal change ($1/N^{1/2}$) that can be then detected at that rate. We have shown that these types of scans can be used to record action-potential-evoked calcium transients in a set of neurons. A high signal to noise ratio is obtained and long recordings can be achieved. The possibility to optimize the illumination for each point, in order to maximize the signal to noise ratio with a minimum photobleaching, is also of particular interest.

We have demonstrated that the use of AODs as scanning system is possible in TPSM. Full compensation of the spatial dispersion can be achieved using an additional AOM. It restores an optimal resolution and two-photon excitation at the center of field of view with minimal distortion on its edge. Optical recordings of electrical activity of neuronal networks in slices and in vivo could take great advantage of this type of scanning.

Acknowledgments

We thank Anne Feltz, Jens Eilers and Luca Guidoni for fruitful discussions. We are grateful to Olivier Crégut for lending us his auto-correlator. This work has been supported by a "Human Frontier Science Foundation" research grant, by the "Ministère de la Recherche et de l'Enseignement Supérieure" (Actions Concertées Incitatives Jeunes Chercheurs 1999), the CNRS (Programme Physique et Chimie du Vivant 1997, Programmes Ultimatech 1997 and 1998), the SPM department of CNRS (Projet jeune chercheur 1999, ATIP jeune chercheur 2002), the French-Israeli Collaboration Program Arc en ciel 2001/02 and the TMR Marie Curie Research Training Grant.

References

Bullen A, Saggau P. High-speed, random-access fluorescence microscopy: II. Fast quantitative measurements with voltage-sensitive dyes. Biophys J 1999;76:2272–87.

Bullen A, Patel SS, Saggau P. High-speed, random-access fluorescence microscopy: I. High-resolution optical recording with voltage-sensitive dyes and ion indicators. Biophys J 1997;73:477–91.

Denk W, Piston DW, Webb WW. Two-photon molecular excitation in laser-scanning microscopy. In: Pawley JB, editor. Handbook of biological confocal microscopy. New York: Plenum; 1995. p. 445–58.

Dunn AK, Wallace VP, Coleno M, Berns MW, Tromberg BJ. Influence of optical properties on two-photon fluorescence imaging in turbid samples. Appl Opt 2000;39:1194–201.

Fan GY, Fujisaki H, Miyawaki A, Tsay RK, Tsien RY, Ellisman MH. Video-rate scanning two-photon excitation fluorescence microscopy and ratio imaging with cameleons. Biophys J 1999;76:2412–20.

Fork MGordon. Negative dispersion using pairs of prisms. Opt Lett 1984;9:150–2.

Goslin K, Banker G. Rat hippocampal neurons in low density culture. In: Banker G, Goslin K, editors. Culturing nerve cells. Cambridge: MIT Press; 1991. p. 251–81.

Helmchen F, Denk W. New developments in multiphoton microscopy. Curr Opin Neurobiol 2002;12:593–601.

Helmchen F, Waters J. Ca^{2+} imaging in the mammalian brain in vivo. Eur J Pharmacol 2002;447:119–29.

Iyer V, Losavio BE, Saggau P. Compensation of spatial and temporal dispersion for acousto-optic multiphoton laser-scanning microscopy. J Biomed Opt 2003;8:460–71.

Lechleiter JD, Lin DT, Sieneart I. Multi-photon laser scanning microscopy using an acoustic optical deflector. Biophys J 2002;83:2292–9.

Muller M, Squier J, Wolleschensky R, Simon U, Brakenhoff GJ. Dispersion pre-compensation of 15 femtosecond optical pulses for high-numerical-aperture objectives. J Microsc 1998;191:141–50.

Ngoi. Angular dispersion compensation for acousto-optic devices used for ultrashort-pulsed laser micromachining. Opt Expr 2001;9:200–6.

Oheim M, Beaurepaire E, Chaigneau E, Mertz J, Charpak S. Two-photon microscopy in brain tissue: parameters influencing the imaging depth. J Neurosci Methods 2001;111:29–37.

Oron D, Tal E, Silberberg Y. Scanningless depth-resolved microscopy. Opt Expr 2005;13:1468–76.

Peterlin ZA, Kozloski J, Mao BQ, Tsiola A, Yuste R. Optical probing of neuronal circuits with calcium indicators. Proc Natl Acad Sci USA 2000;97:3619–24.

Roorda RD, Hohl TM, Toledo-Crow R, Miesenbock G. Video-rate nonlinear microscopy of neuronal membrane dynamics with genetically encoded probes. J Neurophysiol 2004;92:609–21.

Smetters D, Majewska A, Yuste R. Detecting action potentials in neuronal populations with calcium imaging. Methods 1999;18:215–21.

Soeller C, Cannell MB. Construction of a two-photon microscope and optimisation of illumination pulse duration. Pflugers Arch 1996;432:555–61.

Straub M, Lodemann P, Holroyd P, Jahn R, Hell SW. Live cell imaging by multifocal multiphoton microscopy. Eur J Cell Biol 2000;79:726–34.

Theer P, Hasan MT, Denk W. Two-photon imaging to a depth of 1000 micron in living brains by use of a Ti:Al_2O_3 regenerative amplifier. Opt Lett 2003;28:1022–4.

Tsien RY, Bacskai BJ. Video-rate confocal microscopy. In: Pawley JB, editor. Handbook of biological confocal microscopy. New York: Plenum; 1995. p. 459–78.

Wier WG, Balke CW, Michael JA, Mauban JR. A custom confocal and two-photon digital laser scanning microscope. Am J Physiol Heart Circ Physiol 2000;278:H2150–6.

Wyart C, Ybert C, Bourdieu L, Herr C, Prinz C, Chatenay D. Constrained synaptic connectivity in functional mammalian neuronal networks grown on patterned surfaces. J Neurosci Methods 2002;117:123–31.

Yariv A. Optical electronics in modern communications. Oxford: Oxford University Press; 1997.

Yuste R, Lanni F, Konnerth A. Imaging neurons: a laboratory manual. Cold Spring Harbor: Cold Spring Harbor Laboratory Press; 2000.

Zipfel WR, Williams RM, Webb WW. Nonlinear magic: multiphoton microscopy in the biosciences. Nat Biotechnol 2003;21:1369–77.